Fourth and Fifth harmonic generation by Total Internal Reflection – quasi phase matching using the light of highly multimodal nonlinear guided wave approach in a parallel slab of Magnesium oxide doped lithium niobate

JAYA SAHA*, SUMITA DEB
Department of Electrical Engineering, National Institute of Technology, Agartala, Barjala, Jirania, Tripura (west), Pin-799046, Tripura, India

Highly multimodal nonlinear guided wave approach based on Fourth and Fifth harmonic frequency conversion schemes using Total Internal Reflection Quasi phase matching is analytically described in a parallel slab geometry of magnesium oxide doped lithium niobate crystal. The guided wave optics approach provides more accurate and realistic results in comparison to plane ray optics. Effect of nonlinear law of reflection along with other optical losses like absorption, Goos – Hänchen -shift and reflection has also been taken into consideration while calculating the conversion efficiency. Various parametric changes, like variations in slab length and thickness, have also been studied. This scheme significantly improved the conversion efficiency compared to other approaches (e.g., Cascaded generation, periodic polling) utilized for the fourth-harmonic frequency conversion scheme. The conversion efficiency of 0.15418% and 0.00859%, corresponding to the Fourth and Fifth harmonic wavelength of 550 nm and 588 nm, have been observed in a 5 mm and 5.2 mm long crystal, respectively.

(Received March 11, 2024; accepted February 3, 2025)

Keywords: Fourth harmonic generation, TIR-QPM, Parallel slab, Uniaxial crystal, MgO: LN, Waveguide, Non-linear guided wave theory

1. Introduction

Nonlinear optics has developed into a prevalent and efficient technique for extending the frequency range of lasers from the ultraviolet to the visible, infrared, and terahertz ranges, as well as for generating coherent light sources over a wide bandwidth and ultrafast pulse lasers [1,2]. The interaction of laser light, either continuous or pulsed, with nonlinear crystals, leads to the achievement of these phenomena. Up-conversion techniques like Fourth-harmonic (FH) generation and Fifth-harmonic (FTH) generation make it possible to extend to shorter wavelength ranges. FH generation is an effective approach for generating compact coherent light sources at new and shorter wavelengths. It is generally done by two stage-cascaded nonlinear interactions, which involve frequency doubling of the fundamental wavelength, followed by second-harmonic generation in two consecutive crystals [2,3]. FH frequency conversion can also be achieved by another alternative technique known as the Quadrature frequency conversion scheme, where two nonlinear crystals are needed for each step of frequency conversion [3]. As multiple crystals are utilized in the frequency conversion process, it becomes more complex to achieve phase-matching configuration [2]. FH generation by a cascaded process in a single crystal is reported by Brett A. Hooper et al. [4] in $LiNbO_3$, where conversion efficiency is 3.3×10^{-6}.

Akhmanov et al. [5] first reported the FH frequency conversion scheme in a single lithium formiate crystal by using effective fourth-order nonlinearity. Quasi-phase match (QPM) based direct FH frequency conversion in periodically poled $LiNbO_3$ crystal was also reported by Xianfeng Chen et al. [6]. Thus, FH frequency conversion can be obtained using materials with fourth-order optical nonlinear $\chi^{(4)}$ susceptibility. In case of QPM based FH generation in a nonlinear optical material with periodic poling, the fabrication of crystals with high and reliably confirmed quality is challenging and is possible only with certain crystal materials with fairly limited thickness. In a parallel plate, QPM can be achieved by TIR, which was first suggested by Armstrong et al. [5] in 1962. Resonant TIR-QPM based second harmonic generation has been demonstrated in isotropic semiconductors (GaAs, ZnSe, ZnS) by Boyd and Patel [7] as well as by Komine et al. [8]. In the same manner, non-resonant TIR-QPM for difference frequency generation in isotropic semiconductors has been reported by Haïdar et al. [9] .

Harmonic frequency conversion scheme has been demonstrated analytically in this paper by utilizing the concept of Guided Wave Optics based TIR-QPM in a parallel anisotropic crystal slab made of Magnesium oxide (MgO) doped Lithium niobate (MgO:LN) material. In

order to satisfy the ever-increasing demand for wavelength conversion, nonlinear optical crystals have been developed. These crystals include MgO:LN, beta barium borate (BBO), potassium titanium oxide phosphate (KTP), lithium triborate (LBO), potassium dihydrogen phosphate (KDP), and lithium tantalate ($LiTaO_3$) [10]. One of the most advanced and versatile nonlinear optical materials among them is MgO: LN[11]. It is also referred to as "the silicon of nonlinear optics." The fundamental material properties of MgO: LN have the potential to be utilized in a wide variety of applications in the real world [12]. The TIR coefficients are reduced on rough surfaces due to the light scattering that occurs during reflection [10,11]. The pv value of MgO:LN is lower than that of BBO[11]. When comparing MgO:LN to BBO, the effect of surface roughness is thus minimal. Therefore, Mgo:LN has been selected in this study. The Guided wave approach provides more accurate results compared to plane ray optics [9,13]. The effect of various limiting factors, i.e., linear absorption, surface roughness, Goos – Hänchen (GH) shift, and finally, the interference arising due to nonlinear law of reflection (NLR), has been considered to obtain a more realistic approach for the proposed frequency conversion scheme. The effect of variation in slab length and thickness on the resultant harmonic frequency conversion scheme has also been studied in this analysis.

2. Proposed scheme

In this paper, FH and FTH generation has been demonstrated analytically in a parallel slab geometry of MgO:LN by using the phenomena of TIR-QPM through a guided wave approach. With a Gaussian beam as the input source, the experimental setup for the suggested frequency conversion technique is depicted in Fig. 1.

For the generation of FH, a continuous laser source configured to 2200 nm (or 2128 nm) utilized, whereas for the generation of FTH, a laser which is tuned to 2940 nm is utilized. The collimated light beam, which has a beam waist of 100 µm, is focused by an input coupling right angle prism which is situated at the top of the MgO:LN slab, and it is then permitted to propagate through the MgO:LN slab. A right-angle prism that is capable of coupling output may be utilized for the purpose of capturing the generated beam, while a Glass filter can be employed for selectively choosing the generated beam. The Harmonic beam could be captured by cameras that are fitted with charge-coupled devices at the focal length of the lens. In this parallel slab geometry, fundamental optical radiation of frequency ω having incident angle $\emptyset_i$ with respect to the normal on the horizontal base of input coupling prism and thus refracted depending on the index of refraction of the selected material, i.e., MgO: LN. Refraction angle $\emptyset_r$ is calculated from Snell's law of refraction, and it is given as

$$\varphi_r = \sin^{-1}\left(\frac{\varphi_i}{n}\right)$$

Here, n denotes the index of refraction of the chosen material (MgO: LN) for the corresponding fundamental and harmonic frequency, and it has been calculated from the standard Sellmeier Equation.

Therefore, the incidence angle θ_i at the bounce point inside the slab is given as

$$\theta_i = \varphi_r$$

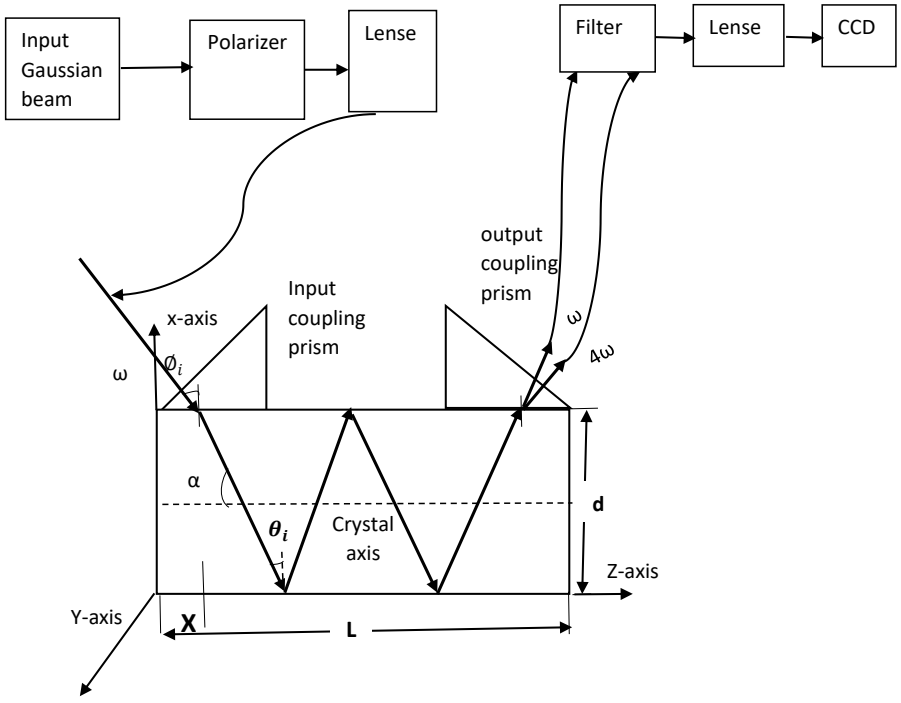

Fig. 1. The geometry of the parallel slab represents the frequency conversion scheme

Now, if the angle of incidence inside the slab is greater than the respective critical angle for both fundamental and harmonic frequency, then the collimated optical radiations will go through repeated TIR inside the slab. The geometrical path length between successive bounces, also the incident angle for both the fundamental and harmonic waves remains the same throughout the slab length L as well, due to the parallelism of the geometry of the proposed slab. Type-I polarization configuration has been performed in this analysis where fundamental and harmonic waves are p and s polarized, respectively.

3. Analysis of multi-mode by nonlinear guided wave approach

The nonlinear guided wave approach has been considered in this analysis to achieve the performance of the proposed FH and FTH frequency conversion scheme. As large number of modes are involved in the wave propagation within the guide, in the beginning, the guide wave method seems to be ineffective. But even if many hundred modes are envisaging through d, typically only a few tens of modes are actually taking part in the process [9,13]. Type 1 polarization configuration has been considered in this analysis where fundamental and harmonic waves are p and s polarized, respectively.

s designates the polarization that is orthogonal to the plane of incidence and p the one that is parallel, one gets the following cases [9,14]:

type 0 phase matching: ppppp, sssss

type I phase matching: pssss, spppp

type II phase matching: pppps, ssssp

The direction of waves propagation and polarization vectors are considered along the x and y axes, respectively. The fundamental and harmonic field function for the parallel slab configuration can be written as [9]

$$\mathrm{H_y^{\omega}(x,z,t)} = \sum_f A_f^{\omega}(z) H_f^{\omega}(x) e^{-i(\omega t-\beta_f^{\omega} z)} e_y + cc \qquad (1)$$

$$\mathrm{E_y^{m\omega}(x,z,t)} = \sum_h A_h^{m\omega}(r,z) E_{h,y}^{m\omega}(x) e^{-i(m\omega t-\beta_h^{m\omega} z)} e_y + cc \qquad (2)$$

Here, m=4,5.

where, varying amplitudes for the input mode f_1 and output mode m are represented by $A_{f_1}^{\omega}(z)$ and $A_h^{m\omega}(z)$ respectively. $H_{f_1}^{\omega}(x)$ and $E_h^{m\omega}(x)$ represents the f_1^{th} and h^{th} order TM(p) and TE (s) wave function for input and output, respectively.

The wave equation follows directly from Maxwell's equations for the perturbed case and can be written as [9,15]

$$\nabla^2 E_y(r,t) = \mu\varepsilon \frac{\partial^2 E_y}{\partial t^2} + \mu \frac{\partial^2}{\partial t^2}[p_{NL}(r,t)] \qquad (3)$$

Complex amplitude of nonlinear polarization terms for frequency conversion scheme can be written as [2]

$$P_{NL} = \varepsilon_0 \chi^{(m)} (E_x^{\omega})^m \qquad (4)$$

and, $$E_x^{\omega}(x,z,t) = \frac{\beta}{\omega\varepsilon} H_y^{\omega}(x) e^{i(\omega t-\beta z)} \qquad (5)$$

In the approximation of un-depleted pump, the equation of coupling mode between the fundamental and the harmonic waves can be derived from equations (1), (2), (3), (4) and (5) as [Appendix A]

$$A_{h,y}^{4\omega}(x) = -i\frac{\varepsilon_0(\beta_f^{\omega})^4}{\omega^3\varepsilon^4 p_0}\int_0^L \sum_{f_1}\sum_{f_2}\sum_{f_3}\sum_{f_4}\{\chi^{(4)} S_{f_1,f_2,f_3,f_4,h}(A_{f_1}^{\omega}, A_{f_2}^{\omega}, A_{f_3}^{\omega}, A_{f_4}^{\omega}) \exp(-i\partial\beta_{f_1,f_2,f_3,f_4,h}L)\}dz \qquad (6)$$

$$A_{h,y}^{5\omega}(x) = -i\frac{\varepsilon_0(\beta_f^{\omega})^5}{\omega^4\varepsilon^5 p_0}\int_0^L \sum_{f_1}\sum_{f_2}\sum_{f_3}\sum_{f_4}\sum_{f_5}\{\chi^{(5)} S_{f_1,f_2,f_3,f_4,f_5,h}(A_{f_1}^{\omega}, A_{f_2}^{\omega}, A_{f_3}^{\omega}, A_{f_4}^{\omega}, A_{f_5}^{\omega}) \exp(-i\partial\beta_{f_1,f_2,f_3,f_4,f_5,h}L)\}dz \qquad (7)$$

Here, Normalized power constant is given by $\mathrm{p_0}$ and it is corresponding to 1 W/m in the y-direction. Therefore, $\mathrm{p_0}$ can be expressed as

$$\mathrm{p_0} = \prod = \frac{1}{\mu_0}\int_{-\infty}^{\infty} E.B\,dx = \frac{\beta_f^{\omega}}{2\omega_m\mu_0}\int_{-\infty}^{\infty}\left|E_{h,y}^{\omega_m}\right|^2 dx \qquad (8)$$

The overall integral for the FH and FTH generation scheme is given by this equation: [Appendix A, Eq. (A.15) and Eq. (A.16)]

$$S_{f_1,f_2,f_3,f_4,h} = 64\sqrt{\frac{\mu_0}{\beta_{f_1\infty}^{\omega}\beta_{f_2\infty}^{\omega}\beta_{f_3\infty}^{\omega}\beta_{f_4\infty}^{\omega}\beta_{h\infty}^{4\omega}}}\left(\frac{\omega p_0}{d}\right)^{5/2}\varepsilon^2\int_{-d/2}^{d/2} sc(f_1\frac{\pi}{d}x)sc(f_2\frac{\pi}{d}x)sc(f_3\frac{\pi}{d}x)sc(f_4\frac{\pi}{d}x)sc(h\frac{\pi}{d}x)dx \qquad (9)$$

$$S_{f_1,f_2,f_3,f_4,f_5,h} = 64\sqrt{\frac{5\mu_0}{\beta_{f_1\infty}^{\omega}\beta_{f_2\infty}^{\omega}\beta_{f_3\infty}^{\omega}\beta_{f_4\infty}^{\omega}\beta_{f_5\infty}^{\omega}\beta_{h\infty}^{5\omega}}}\left(\frac{\omega p_0}{d}\right)^3\varepsilon^{5/2} \int_{-d/2}^{d/2} sc(f_1\frac{\pi}{d}x)sc(f_2\frac{\pi}{d}x)sc(f_3\frac{\pi}{d}x)sc(f_4\frac{\pi}{d}x)sc(f_5\frac{\pi}{d}x)sc(h\frac{\pi}{d}x)dx \qquad (10)$$

Here, sc is the sine function if f_1 is even (odd modes) and cosine if f_1 is odd (even modes). For very large values of modes 'f_1' and 'm', the overall integral is non-zero and it is only if $f_1 + f_2 + f_3 + f_4 - h = \Delta$, Δ being mode mismatch. In addition, for small values of Δ ($|\Delta| = 1$), the overall integral becomes more intensified. However, larger values of Δ tends to increase the non-collinearity

angle among the interacting waves, resulting in lower spatial overlap.

Again now, propagation constants mismatch is and it is given by $\partial\beta_{f_1,f_2,f_3,f_4,h}$

$$\partial\beta_{f_1,f_2,f_3,f_4,h} = \beta_{f_1}^{\omega} + \beta_{f_2}^{\omega} + \beta_{f_3}^{\omega} + \beta_{f_4}^{\omega} - \beta_h^{\omega_4}$$

where, $\beta_{f_\cdot}^{\omega} = \sqrt{(n_\omega k_\omega)^2 - (f_g \frac{\pi}{d})^2 \exp(\frac{-2}{K_{f_g} v_\omega})}$ and

$$\beta_h^{\omega_m} = \sqrt{(mn_{m\omega}k_\omega)^2 - (h\frac{\pi}{d})^2 \exp(\frac{-2}{K_h v_{\omega_m}})}$$

Here, g=1, 2, 3, 4,5 and K_{f_g} =1 for TE polarization and for TM polarization which implies the effect of Fresnel birefringence. The transverse and evanescent wavenumber for a waveguide thickness of 'd' has been given by [9]

$$\left.\begin{aligned} \alpha_{f_g}^{\omega} &= \sqrt{(n_\omega k_w)^2 - (\beta_{f_g}^{\omega})^2} \\ k_{f_g}^{\omega} &= \sqrt{(\beta_{f_g}^{\omega})^2 - (k_\omega)^2} \end{aligned}\right\} \quad (11)$$

$\beta_{f_g}^{\omega}$ can be obtained by using the equations (11) and (12) [13]

$$\tan(\alpha_{f_g}^{\omega} d) = \frac{2k_{f_g}^{\omega}\alpha_{f_g}^{\omega}}{(\alpha_{f_g}^{\omega})^2 - (k_{f_g}^{\omega})^2}. \quad (12)$$

The mode amplitude $A_{f_g}^{\omega}$ can be expressed by this equation [11]:

$$A_{f_g}^{\omega} = 2iL\sqrt{\frac{\omega\mu_0}{\beta_{f_g} d}}\, p_0 \frac{\sqrt{\pi}}{2\omega} \sin\theta e^{-F(f)^2} \times \left[Erfi\{F(f_g) - i\frac{\sin\theta}{2}\frac{d}{\omega_0}\} - Erfi\{F(f_g) + i\frac{\sin\theta}{2}\frac{d}{\omega_0}\} \right] \quad (13)$$

Here, ω_0 is beam waist of fundamental gaussian beam and the function $F(f_g)$ is given by this equation [9]

$$F(f_g) = \frac{1}{2}\frac{\omega_0}{\sin\theta}(k_\omega \cos\theta - f_g \frac{\pi}{d}) \quad (14)$$

And $Erfi(z) = -iErf(iz)$, $Erf(z)$ represents the error function [11].

For a given angle of incidence θi, $A_{f_g}^{\omega}(0)$ is become maximum at $f_g \sim f_{\theta_i}$, allowing about 10-20 modes to participate in a large number of modes. In general, these few tens of modes should be enough for the input laser beam [9,13] to be guided through the parallel slab geometry. Equation (13) implies that the propagation of Gaussian beam is focused around $l_\theta \approx \cos\theta \frac{k_\omega d}{\pi}$. Also, the amplitude of mode is highest for $F(f_g) = 0$. In order to guiding wave, this condition must exist for an infinitely confining waveguide (ICW) [13]. In addition, the number of modes in excitation is approximately given by $\Delta l \approx \frac{4d\sin\theta}{\pi\omega_0}$.

Some numerical decompositions have been done here to understand roughly how many modes can be accommodated in the guide. For this, V-number has also been calculated, and it is given by $V = k_0 d\sqrt{n_1^2 - n_2^2}$. Here, k_0 represents the wavenumber of the fundamental beam, t is the slab thickness, n_1 is the index of refraction of the MgO: LN and n_2 is the index of refraction of air. $n_1 = n_3$ for a symmetric slab.

Therefore, from equation (15) number of TE or TM modes in total can be the obtained as [13]

$$N = \left[\frac{1}{\pi}\{V - \tan^{-1}\frac{\eta(n_2^2 - n_3^2)^{\frac{1}{2}}}{(n_1^2 - n_2^2)^{\frac{1}{2}}}\} \right]_{\text{int}} \quad (15)$$

Here the parameter η =1 for TE modes and $\eta = \frac{n_1^2}{n_3^2}$ for TM modes. Also, N represents an integer, whose value must be just greater than the value of the number in brackets.

Now, it has been observed that $\frac{V}{\pi}$ ~303 for fundamental input wavelength of 2.128 μm and slab thickness of 150 μm. Additional criteria that must be fulfilled is:

$$\begin{aligned} &\{(2n+1)\}\pi < V < \{(2n+2)\}\pi \\ &= \{(2\times\frac{302}{2}+1)\}\pi < V < \{2\times\frac{302}{2}+2)\}\pi \\ &= 303\pi < V < 304\pi \end{aligned}$$

Accordingly, $\frac{V}{\pi}$ can be calculated as 303 or 304.

In this analysis, it has been found that asymmetrical modes are n' =151, and symmetrical modes are $n'+1$ =152. Therefore, 10-20 modes have been taken in this analysis to describe the nonlinear guided wave approach for the FH frequency conversion scheme.

Here, the optic axis is not parallel to the propagation vector of generated harmonic. Therefore, there is a propagation of the component wave (p and s) of the generated harmonic field $E_y^{h\omega}$ resulting in an additional phase shift of the component wave during consecutive bounces. Now, the Jones Vector concept has been used to

determine the component of wave $E_y^{m\omega}$ (p and s) in terms of Rotation Matrix R(α) [16] as follows,

$$R(\alpha)=\begin{bmatrix} cos\alpha & sin\alpha \\ -sin\alpha & cos\alpha \end{bmatrix} \quad (16)$$

For TIRQPM

$$\begin{bmatrix} E_{y\text{-}p}^{m\omega} \\ E_{y\text{-}s}^{m\omega} \end{bmatrix}=\begin{bmatrix} cos\alpha & sin\alpha \\ -sin\alpha & cos\alpha \end{bmatrix}\begin{bmatrix} 0 \\ 1 \end{bmatrix}=\begin{bmatrix} sin\alpha \\ cos\alpha \end{bmatrix} \quad (17)$$

The electric vector of a linear polarized wave is represented by the jones vector $\rho_{y=}\begin{bmatrix} 0 \\ 1 \end{bmatrix}$, which works in the execution of a simple harmonic oscillation along the y axis having a zero phase with unit amplitude [16].

The effect of TIR has been incorporated for generating FH and FTH. The harmonic electric field for any intermediate length L_j (j>1) for s and $L_{j-1}(j>0)$ p wave can be written as [17],

$$E_{y\_s(TIRQPM)}^{m\omega}(L_j)=\{e^{-i\Delta\phi_1}cos\alpha+e^{-i\Delta\phi_2}cos^2\alpha+\ldots.+ e^{-i(j-1)\Delta\phi_{(j-1)}}cos^{(j-1)}\alpha\}\,E_{y\_s}^{m\omega}(L_1) \quad (18)$$

$$E_{y\_p(TIRQPM)}^{m\omega}(L_{j-1})=\{e^{-i\Delta\phi_1}sin\alpha+e^{-i\Delta\phi_2}sin^2\alpha+\ldots.+ e^{-i(j-1)\Delta\phi_{(j-1)}}sin^{(j-1)}\alpha\}\,E_{y\_p}^{m\omega}(L_1) \quad (19)$$

The net electric field of harmonic for n number of bounces is given by

$$E_y^{m\omega}(L_1+L_2+\ldots..+L_n)=\sum_{j=1}^{n}\{E_{y\_s(TIRQPM)}^{m\omega}(L_j)+E_{y\_p(TIRQPM)}^{m\omega}(L_{j-1})\} \quad (20)$$

In terms of net harmonic electric field, the time-average harmonic intensity I_m can be expressed as

$$I_m=\frac{n_m c}{8\pi}E_y^{m\omega}E_y^{m\omega^*} \quad (21)$$

Finally, conversion efficiency is expressed as

$$\eta_{con}=\frac{I_m}{I_1}\times 100\% \quad (22)$$

where, I_1 is the fundamental input intensity.

4. Conversion yield limiting factors

The efficiency of the frequency conversion scheme is limited by certain important factors, namely surface roughness, GH shift, absorption loss of the material, and diffraction due to NLR.

4.1. Surface roughness

Depending on the surface roughness, whenever a beam of light reflects from an interface, then it undergoes a phase shift. This deviation has two likely effects. Firstly, it initiates a noise on Fresnel phase shift which can be completely neglected, as the roughness is of the order of a few nm. Secondly, the roughness generates a dispersion of light. This finally leads to lowering down TIR coefficient (measured in terms of Strehl ratio).

Light reflected having reflection coefficient R is a measure of drop, and it is a function of angle of incidence and input wavelength [9]

$$R=\exp[-(\sigma\frac{4\pi n}{\lambda}\cos\theta_i)^2]\approx 1-(\sigma\frac{4\pi n}{\lambda}\cos\theta_i)^2 \quad (23)$$

We have assumed γ=pv value and $\sigma=\frac{\gamma}{12}$. A pv value of 6 nm has been taken into consideration for incorporating the effect of surface roughness [11].

4.2. GH shift

During Total internal reflection of the collimated light beam between two dielectric media, the reflected beam undergoes a longitudinal shift between the incident and reflected beams is expressed as [18]

$$S^E=\left(\frac{2}{k_i}\right)\frac{tan\theta_{cri}}{(sin^2\phi-sin^2\theta_{cri})^{1/2}} \quad (24)$$

$k_i=2\pi n_i/\lambda_i$

Here, k_i is the wave vector of vacuum wavelength λ_i, n_i is the index of refraction of denser media, ϕ is the angle of incidence, and θ_{cri} is the critical angle. Due to the GH shift, there will be a reduction in the usable length of the crystal. In this analysis, the shift has been computed for both upper and lower surfaces. Therefore, the pump wavelength of 2200 nm has encountered a GH shift of 1.8 μm for the corresponding slab length of 8 mm.

4.3. Absorption

Linear absorption can be very harmful to frequency conversion and severely limits the conversion efficiency. Typically, linear absorption coefficients, (α'_ω and $\alpha'_{4\omega}$) is much less than 1. Usually, absorption of the fundamental cannot be entirely eliminated; however, at very low absorption, it is sometimes masked by scattering. Absorption has another harmful effect on material heating. Absorption can also generate a drift in the phase matching conditions and a drop in conversion efficiency [9].

4.4. Diffraction due to NLR

According to NLR, a homogeneous FH field is generated at the interface by the nonlinear polarization vector in addition to the generation of the collinear FH

field in order to satisfy the conservation of wave momentum parallel to the boundary [19]. It follows the Snell – Descartes principle:

$$n_{\omega} \sin\theta_{\omega} = n_{4\omega} \sin\theta_{4\omega} \quad (25)$$

where n_{ω} and $n_{4\omega}$ are the refractive indices at the fundamental and generated FH respectively, θ_{ω} and $\theta_{4\omega}$ are the incidence angles of fundamental and FH, respectively.

The angle variation between the colinear and homogeneous FH wave is given as [20]

$$\delta\theta \approx -(\delta n / n)\tan\theta_{\omega} \quad (26)$$

Here, $\delta n = n_{4\omega} - n_{\omega}$ is the optical dispersion, and $n \approx n_{4\omega} \approx n_{\omega}$.

$$N_{rec} \approx 2|\tan\theta_{\omega}/\delta\theta| \approx 2|n/\delta n| \quad (27)$$

This non-collinearity has two effects: first, spatial walk-off and second, the recombination between the field wave inside the slab, which gives the destructive or constructive interference at different bounce points. Fig. 2 shows the impact of NLR.

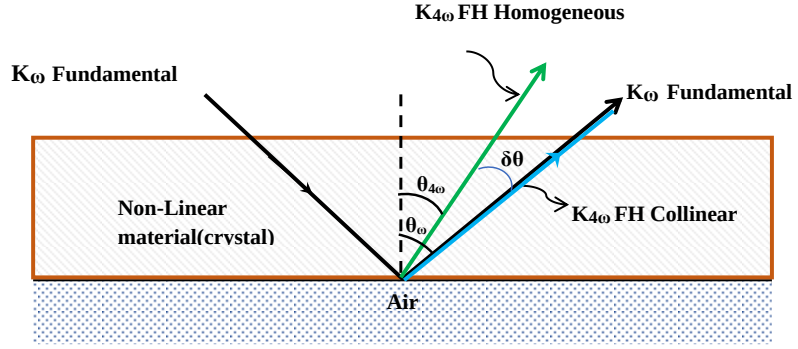

Fig. 2. Generation of collinear and "homogeneous" FH waves at the air-crystal interface according to law of Non-linear Reflection (colour online)

5. Simulation results and discussions

The computer-aided simulation for the parallel slab In the computer-aided simulation, the input fundamental beam intensity has been assumed as Iω = 7.5 MW/cm^2 with due consideration of the damage threshold value of MgO: LN [18]. The material that is chosen is MgO:LN, an anisotropic material. For the FH frequency conversion with FH wavelength of 550 nm, all bounce lengths into the parallel slab geometry of MgO:LN have been added up to obtain the total interaction length. The resultant value comes to about 1.031 cm. Rayleigh range has also been computed for the same wavelength for a beam waist of 100 μm which comes out to be 1.3481 cm, thus satisfying the Rayleigh range condition.

Lambda = 2.2 μm, temperature = 298 k, θ_i = 0.478 radian, d=150 μm, x=0.5 μm

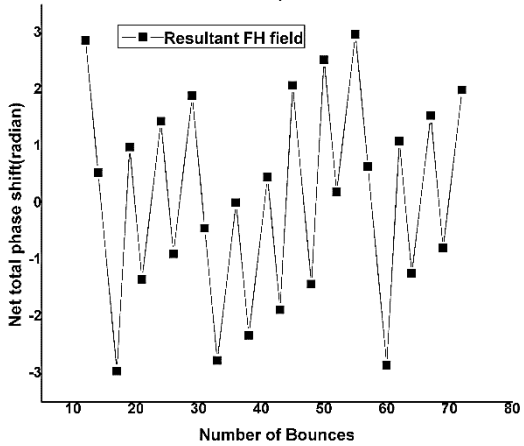

Fig. 3. Variation in Net total phase shift as a function of the number of bounces for generating 550 nm FH wavelength

The efficiency peak is obtained corresponding to an application wavelength of 550 nm is 0.15488%. The effects of variation in slab length and thickness have been studied on the FH conversion efficiency for the parallel slab configuration of MgO:LN under consideration.

According to the TIR-QPM phenomenon, every bounce point of TIR is responsible for the generation of a colinear harmonic field. Each TIR bounce will also generate a homogeneous harmonic due to NLR (Fig. 2). At every bounce location of TIR, two distinct generations of harmonic occur one collinear harmonic generated by second-order interaction that propagates at an angle that is identical to incidence angle, i.e., and another homogeneous harmonic, which travels at an angular shift of with regard to the collinear harmonic. Apart from these two new generations at any given bounce point, the fields that are caused by the harmonics (both collinear and homogeneous) generated at all of the preceding bounce locations, which have experienced Fresnel phase shifts at each consecutive bounce point [9]. At the subsequent bounce point, the harmonic that was generated at the first bounce point will go through a Fresnel phase shift and will correspondingly contribute to the collinear harmonic that is generated at that bounce location of TIR.

After accounting for the relative shift in phase between the two generated harmonic waves, the net field amplitude of harmonic at this bounce point has been determined. The harmonic field at the following bounce point has also been computed because of the generation of collinear and homogenous harmonics. The same process will be repeated at the subsequent bounce point and, so on. Finally, the net electric field generated at the exit point has been obtained by adding the two field contributions, due to

collinear as well as homogenous harmonics, along with their net phase shifts. The effectiveness of the conversion is substantially impacted by the re-combinative phenomena that are caused by the NLR. This recombinant phenomenon illustrates a combination of destructive and constructive interference occurring between the collinear (Each bounce causes a phase change of either 0 or 2π) and homogeneous harmonic (The phase shift undergoes variation from 0 to π while propagating) fields that are generated by the frequency conversion process. As a consequence of these subsequent recombinational events, the radiation efficiency of the system diverges substantially, leading to constructive or destructive interference at respective bounce sites.

5.1. Effect of variation in slab length

During the propagation of the collimated beam inside the parallel slab geometry of MgO: LN, the length between two consecutive bounce points and angle of incidence are fixed at each bounce point. The angle of incidence has been chosen in such a way that the length between two consecutive bounces is equal to an odd integer multiple of the coherence length for the input wavelength under consideration as well as the condition for constructive interference is also satisfied.

By keeping the slab thickness constant throughout this part of the analysis and increasing the slab length, it has been observed that that the peak conversion efficiency increases up to a certain slab length and then starts to fall. Due to the NLR at each bounce point, two FH waves are generated. The angle of separation increases as both waves propagate, creating a spatial walk-off, which reduces the overlapping conditions between the interacting waves. Therefore, when the beam travels through the slab, they tend to have a phase difference of 2π, causing constructive interference and hence an increase in efficiency. Similarly, when the beams tend away from a phase difference of 2π, they undergo destructive interference causing a drop in efficiency.

Fig. 3 shows the variation in the total phase shift of the resultant fourth harmonic field with respect to the number of bounces for generating 550 nm wavelength where the number of TIR bounces increases from 10 to 40 with the increase of slab length from 4 mm to 7 mm. From Fig. 3, it is observed that the net total phase shift for the resultant fourth harmonic field is approximately 0 at 20 and 40 number bounce points. Therefore, constructive interference occurred at 20 and 40 number bounce points. Table 1 and Table 2, along with Figs. 4, 5, 6 and 7, give an illustration of it.

Lambda = 2.2 μm, temperature = 298 k, θ_i =0.478 radian, d = 150 μm, x = 0.5 μm

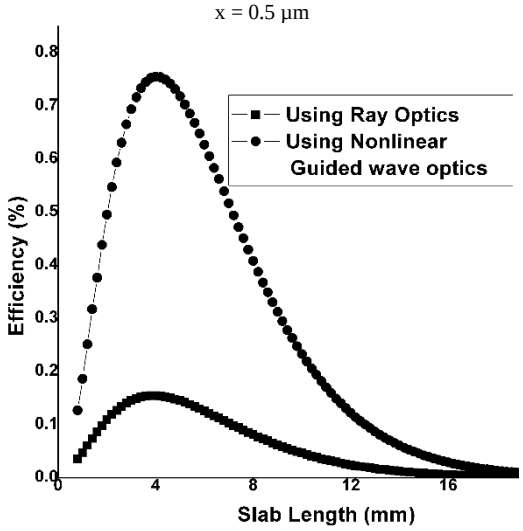

Fig. 4. Variation in efficiency as a function of slab length for generating 550 nm FH wavelength

Lambda=2.2 μm, temperature = 298 k, θ_i = 0.478 radian, d = 150 μm, x = 0.5 μm

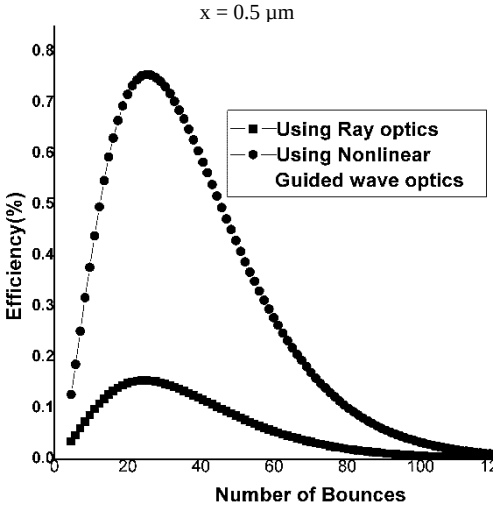

Fig. 5. Variation in efficiency as a function of the number of bounces for generating 550 nm FH wavelength

Lambda = 2.128 μm, temperature = 298 k, θ_i =0.81507 radian, d=150 μm, x=0.5 μm

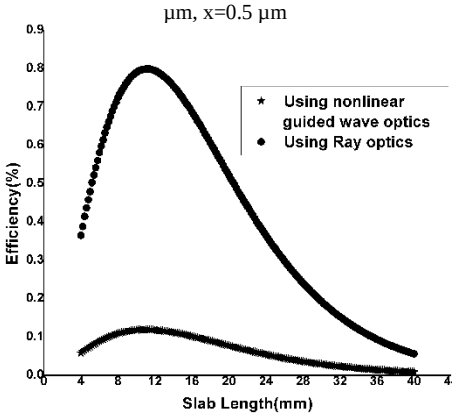

Fig. 6. Variation in efficiency as a function of slab length for generating 532 nm FH wavelength

The impact of increasing the length of the slab for generating 550 nm and 532 nm wavelengths is shown in Figs. 4, 5, 6, and 7. From Figs. 4 and 5, it is observed that constructive interference occurred at the 25th bounce point, i.e., at the slab length of 5 mm, and the maximum efficiency at that bounce point is 0.15488% for generating 550 nm wavelength when nonlinear guided wave approach is considered. In the same way from Figs. 6 and 7, it is observed that maximum efficiency of 0.11872 % is obtained for generating 532 nm wavelength at 34th bounce point, i.e., at slab length of 11 mm. Figs. 8 and 9 have been employed to further analyze the variations in slab length and the number of bounces to generate the 588 nm FTH wavelength. Figs. 8 and 9 demonstrate that constructive interference has occurred at the 16^{th} bounce positions, which correspond to the lengths of the slabs being 5.2 mm.

The effect of slab length variance on the performance parameter has been shown in Table 1.

5.2. Effect of variation in slab thickness

When the thickness of the slab has been varied from 151 to 159 μm in steps of 2 μm, the efficiency under the Ray optics approach and on consideration of the nonlinear guided wave approach decreases with the increase in slab thickness. The decrease in conversion efficiency is due to the decrease in the number of bounces with the increase in slab thickness.

During thickness variation, the angle of incidence has been chosen in such a way that the geometric path length between two consecutive bounce points is equivalent to an odd integer multiple of the coherence length for the input wavelength under consideration, as well as the condition for constructive interference is also satisfied. The angle of incidence during thickness variation is also chosen in such a way that the order of QPM for different application wavelengths of 532 nm, 550 nm 9, 11, respectively, and the maximum efficiency obtained at these wavelengths is 0.10576%, 0.14486%, respectively. The maximum FTH conversion efficiency of 0.00395% has been obtained for the generation of 588 nm wavelength. The effect of thickness variance on the performance parameter has been shown in Table 2.

Table 1. When MgO:LN waveguide is subjected to slab length variation (L). d=150 μm, I_1=7.5 Mw/cm^2, temperature = 298 k, x = 0.5 μm

Input Wavelength (nm)	Output Wavelength (nm)	φ_i (radian)	Slab length (mm)	Efficiency (%)	
				Ray optics Approach	Nonlinear Guided Wave approach
2200	550(FH)	0.4782	4	0.71598	0.14872
			5	0.75477	0.15418
			7	0.66757	0.13381
			8	0.58275	0.11624
			9	0.40785	0.08061
2128	532(FH)	0.81507	5	0.36525	0.05482
			6	0.45784	0.07166
			11	0.79914	0.11872
			15	0.79456	0.11786
2940	588(FTH)	0.496	17.7	0.74894	0.11082
			4	0.02905	0.00803
			5	0.03104	0.00857
			5.2	0.03111	0.00859
			6	0.03048	0.00843

Table 2. When MgO:LN waveguide is subjected to slab thickness variation (d). L=8 mm, I_1=7.5 Mw/cm², temperature = 298 k, x=0.5 µm

Input Wavelength (nm)	Output Wavelength (nm)	φ_i (radian)	Slab thickness (µm)	Efficiency (%)	
				Ray optics Approach	Nonlinear Guided Wave approach
2200	550(FH)	0.4872	151	0.69326	0.14486
		0.64577	153	0.63017	0.13368
		0.76021	155	0.58275	0.11624
		0.84417	157	0.51639	0.10275
		0.73304	159	0.49372	0.09365
2128	532(FH)	0.81507	151	0.70097	0.10576
		0.69639	153	0.67457	0.10242
		0.70511	155	0.61424	0.09372
		0.7278	157	0.5979	0.08655
		0.68591	159	0.50268	0.07465
2940	588(FTH)	0.492	151	0.0189	0.00395
		0.499	153	0.0159	0.00305
		0.497	155	0.011	0.00251

Lambda=2.128 µm, temperature=298k, θ_i =0.81507 radian, d=150 µm, x=0.5 µm

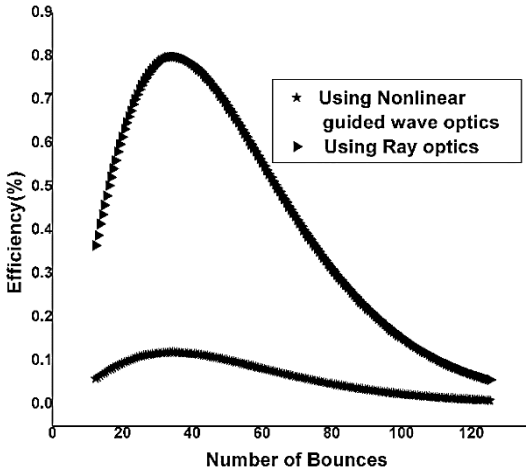

Fig. 7. Variation in efficiency as a function of number of bounces for generating 532 nm FH wavelength

5.3. Effect of variation in beam waist

Varying the beam waist has a considerable impact on the efficiency and stability of the harmonic generating process. Smaller beam waists improve peak intensities, which in turn boosts the efficiency of nonlinear conversion; nevertheless, this can compromise stability due to the difficulties associated with the impacts of thermal effects. An optimized beam waist balances these competing factors, ensuring robust and efficient harmonic generation. A larger beam waist (Fig. 10) results in a lower peak intensity, which in turn leads to a reduction in the efficiency of the conversion.

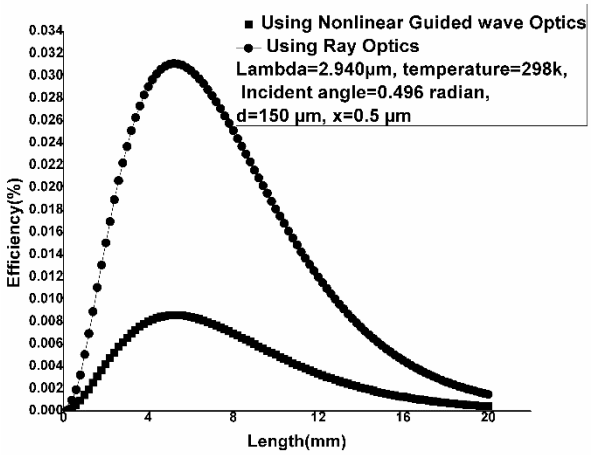

Fig. 8. Variation in efficiency as a function of slab length for generating 588 nm FTH wavelength

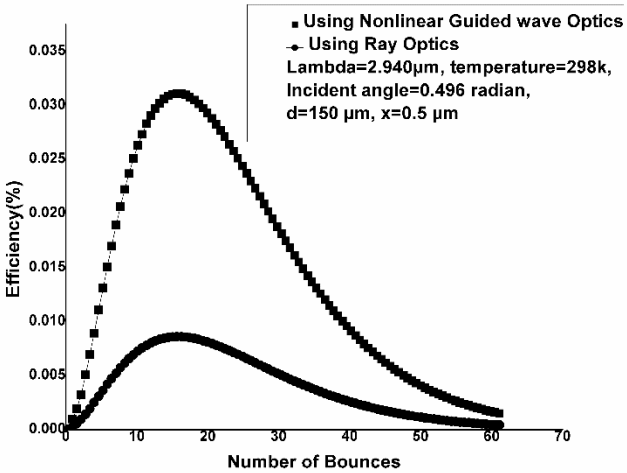

Fig. 9. Variation in efficiency as a function of Number of bounces for generating 588 nm FTH wavelength

6. Discussion

Gaussian lasers are more common and cost-efficient than laser sources with other beam profiles like Laguerre Gaussian beam [21]. Most high-quality, single-mode laser sources emit a beam following a low-order Gaussian irradiance profile, which is also known as the TEM_{00} mode [22,23]. Lower-quality sources will have some level of other laser modes present as well, but it is often assumed that lasers have an ideal Gaussian profile to simplify system modelling [23,24]. In spite of variations in peak value or beam size, the irradiance profile of a Gaussian beam propagating through an optical system remains Gaussian. This means that Gaussian beams remain constant under transformations [22].

Lithium niobate is a popular electro-optic material due to its high birefringence, ferroelectricity, and nonlinear optical characteristics. Photonic devices, waveguides, frequency converters, and optical modulators are some of the most common applications for this material. It has lower resistance to photorefractive damage [26]. MgO doping in $LiNbO_3$ enhances its resistance to photorefractive damage and improves thermal stability, making it suitable for high-power applications. Typical MgO doping levels range from 5 to 7 mol%. Maintaining 5–7 mol% MgO ensures optimal photorefractive resistance. Maintaining 5–7 mol% MgO ensures optimal photorefractive resistance [12,25]. The primary method for preparing MgO:LN crystals is the Czochralski method. Several methods, including Proton Exchange (PE), Direct Laser Writing, Ion Implantation, can be utilized in order to fabricate waveguides of MgO:LN. Precise temperature management is critical for stoichiometric composition during crystal growth [11,26]. Annealing removes internal stress and defects, improving optical quality. Proper cladding ensures confinement of light within the waveguide [15].

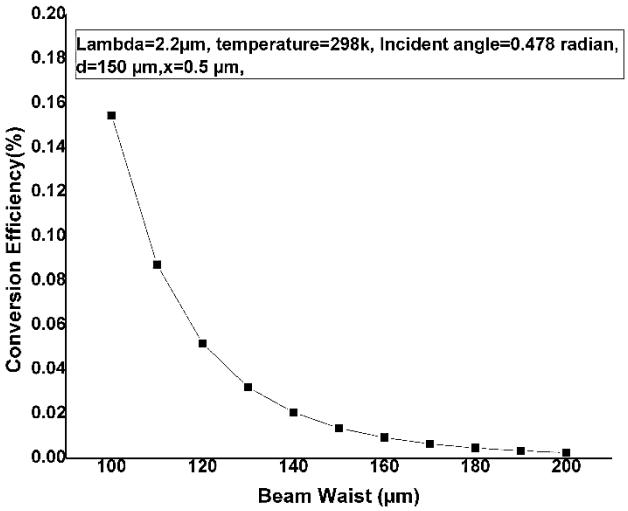

Fig. 10. Variation in efficiency as a function of beam waist for generating 550 nm FH wavelength

Table 3. Comparison of the proposed technique with the reported processes

SL NO.	**Phase matching Process**	**Crystal material**	**Input wavelength**	**No. of crystal**	**Crystal length**	**Efficiency (%)**	**Normalized efficiency (%/watt)**	**Reference**
1	QP M	PPKTP	1560 nm (FH)	2	15 mm, 10 mm	10^{-5}~ 10^{-6}	2.5 $\times 10^{-6}$~2.5 $\times 10^{-7}$	[27]
2	Not mentioned	$AgGaSe_2$ $ZnGeP_2$	2.55 μm (FH)	2	20 mm, 10 mm	1.17×10^{-5}	6.88×10^{-6}	[28]
3	Not mentioned	$LiNbO_3$	2 μm (FH)	1	1 cm	3.3×10^{-6}	3.458×10^{-9}	[4]
4	QPM	Periodically poled $LiNbO_3$	3797 nm (FH)	1	1 cm	Not mentioned	Not mentioned	[6]
5	TIR-QPM	MgO: LN	2200 nm (FH) 2128 nm (FH) 2940 nm (FTH)	1 1 1	5 mm 5.1 mm 5.2 mm	0.15418 0.11872 0.00859%	1.3087×10^{-4} 1.0077×10^{-4} 7.29148×10^{-6}	Proposed

The FH and FTH generation wavelength have been selected in such a way that the wavelengths have potential application in medical science as well as the lower order QPM is possible at those wavelengths. As an additional factor to take into account in this work, we analyzed the performance of the frequency conversion system in relation to the varying length and thickness of the slab. In order to maximize the efficiency of frequency mixing and harmonic generation approach, phase-matching is a crucial requirement. The only governing variable that has any

influence either on the global phase shift, or more specifically, the Fresnel phase shift that takes place under TIR, is the incidence angle. For a specific combination of wavelength and polarization state, the additional phase shift, and the dispersion mismatch in phase, ΔKL_b, are both fixed values.

The incidence angle has been tuned so that the resonant QPM criteria and the phase-matching requirement are both met for the specified pump wavelength. The length of the slab has been estimated in such a manner that the total of the interaction lengths inside the slab is smaller than the corresponding value of the Rayleigh range. Furthermore, QPM order is defined as the ratio of the interaction length between two consecutive bounce points to the coherence length for the specific wavelength. The slab thickness and the incidence angle are the two governing parameter that take into consideration when determining the QPM order. QPM conversion efficiency improves as the order decreases. Therefore, in order to achieve a lower-order QPM, a slightly thinner thickness has been taken into account for this analysis. In a gaussian beam-based frequency conversion approach, the diffraction effect of NLR causes the peak conversion efficiency to grow up to a specific slab length, after which it begins to decrease. The peak conversion efficiency of 0.15488% has been observed at 5 mm slab length for generating 550 nm (FH) wavelength.

The effect of limiting factors has been considered in this analysis. The length of the crystal that can be used will be shorter because of the GH shift. A GH shift of 1.8 μm has been observed at the pump wavelength of 2200 nm for the slab length of 8 mm. Light is scattered upon reflection due to the roughness. The TIR coefficient decreases as a result of this. The effect of surface roughness can be minimized by using highly polished surface of the material. Lights are diffracted due to NLR. The impact of NLR in gaussian beam based frequency conversion scheme can be mitigated by using slab lengths that are lower than the Rayleigh range. Also, by employing non-gaussian beam profiles, such as Laguerre-Gaussian or Bessel gauss beams, which are non-diffractive in nature, can reduce the effect of NLR.

7. Conclusion

In this paper, FH and FTH frequency conversion using TIR-QPM and Guided wave approach in a parallel slab geometry of anisotropic material (MgO: LN) has been described analytically. When guided wave analysis is taken into account, the benefit is found because of two reasons – (i) waves exhibiting non-collinearity and (ii) the GH shift accounts in a built-in way, thus providing more realistic results as told by Raybaut et al. [9]. The proposed scheme demonstrates the technologically simple idea of QPM by utilizing TIR phenomena in the geometry of a parallel plate. This scheme has several advantages over the conventional methods, such as cascaded FH generation and quadrature frequency conversion methods that demand the utilization of multiple crystals for the conversion process. TIR-QPM method provides better efficiency as compared to conventional cascaded FH generation in a single crystal. The cascaded FH generation process in a single crystal is reported by Brett A. Hooper et al. [4] in $LiNbO_3$, where conversion efficiency is much less than our proposed frequency converter.

When using the ray-optics approach and limiting factors are considered, in a parallel slab geometry of MgO:LN length of 5 mm, the efficiency is as high as 0.75477 % with fundamental input wavelength at 2.2 μm. Next, with the non-linear guided wave approach (under loss condition), which is a more realistic approach, it has been observed that the efficiency is not as high as that of ray optics. The conversion efficiency comes out to be 0.15418 % for a FH wavelength of 550 nm and 0.00859% for a FTH wavelength of 588 nm. It is to be mentioned here that the effects of absorption loss, reflection loss, Goos-Hänchen shift and NLR are taken into account in the conversion process.

From the application point of view, FH generation using MgO:LN material for generating 532 nm wavelength can be useful in fluorescence spectroscopy, optical alignment, green light illumination, and in some medical applications like treating vascular skin lesions, [29] endoscopy [30]. 550 nm can be used in ozone monitoring instruments, [31] flow cytometry [32]. Also, 588 nm can be used in Light Biosciences [33].

Appendix-A: Computation of the harmonic Field Amplitude

TM Modes

The components of the fields have been defined by taking into account the slowly varying amplitudes of the mode f as,

$$\mathrm{H_y^{\omega}(x,z,t)} = \sum_f A_f^{\omega}(r,z) H_f^{\omega}(x) e^{-i(\omega t - \beta_f^{\omega} z)} e_y + cc \quad \text{(A.1)}$$

$$E_x^{\omega}(x,z,t) = \frac{i}{\omega\varepsilon}\frac{\partial H_y^{\omega}}{\partial z} \quad \text{(A.2)}$$

$$\mathrm{H_x^{\omega}(x,z,t)} = \frac{1}{\omega\varepsilon}\sum_f \beta_f^{\omega} A_f^{\omega}(r,z) H_f^{\omega}(x) e^{-i(\omega t - \beta_f^{\omega} z)} e_y + cc \quad \text{(A.3)}$$

TE Modes

The field function of the generated harmonic field with gradually varying amplitudes of mode h can be expressed as

$$\mathrm{E_y^{m\omega}(x,z,t)} = \sum_h A_h^{m\omega}(r,z) E_{h,y}^{m\omega}(x) e^{-i(m\omega t - \beta_h^{m\omega} z)} e_y + cc \quad \text{(A.4)}$$

Here, m=4,5

In the presence of perturbation, it is possible to derive the wave equation from Maxwell's equation in a direct manner as

$$\nabla^2 E_y(r,t) = \mu\varepsilon\frac{\partial^2 E_y}{\partial t^2} + \mu\frac{\partial^2}{\partial t^2}[p_{NL}(r,t)] \quad \text{(A.5)}$$

The nonlinear polarization amplitude for the perturbed case is given by

$$P_{NL} = \varepsilon_0 \chi^{(m)} (E_x^{\omega})^m \quad \text{(A.6)}$$

Since $\frac{\partial^2 A_h^{m\omega}(z)}{\partial z^2} << \beta_h^{m\omega} \frac{\partial A_h^{m\omega}(z)}{dz}$, we may disregard the term $\frac{\partial^2 A_h^{m\omega}(z)}{\partial z^2}$ for slow variation.

After the first bounce, the coupling mode equation for generated FH field using TIRQPM can be expressed as,

$$\frac{d}{dz} A_{h,y}^{4\omega}(x) = -i \frac{\varepsilon_0 (\beta_f^{\omega})^4}{\omega^3 \varepsilon^4 p_0} \sum_{f_1} \sum_{f_2} \sum_{f_3} \sum_{f_4} \{\chi^{(4)} S_{f_1,f_2,f_3,f_4,h} (A_{f_1}^{\omega} A_{f_2}^{\omega} A_{f_3}^{\omega} A_{f_4}^{\omega}) \exp(-i\partial\beta_{f_1,f_2,f_3,f_4,h} L)\} \quad \text{(A.7)}$$

Following the first bounce, the coupling mode equation for the generated FTH field by the use of TIRQPM can be stated as

$$\frac{d}{dz} A_{h,y}^{5\omega}(x) = -i \frac{\varepsilon_0 (\beta_f^{\omega})^5}{\omega^4 \varepsilon^5 p_0} \sum_{f_1} \sum_{f_2} \sum_{f_3} \sum_{f_4} \sum_{f_5} \{\chi^{(5)} S_{f_1,f_2,f_3,f_4,f_5,h} (A_{f_1}^{\omega} A_{f_2}^{\omega} A_{f_3}^{\omega} A_{f_4}^{\omega} A_{f_5}^{\omega}) \exp(-i\partial\beta_{f_1,f_2,f_3,f_4,f_5,h} L)\} \quad \text{(A.8)}$$

The increment in the amplitude of FH fields along the z-axis can be expressed by using the following integral

$$A_{h,y}^{4\omega}(x) = -i \frac{\varepsilon_0 (\beta_f^{\omega})^4}{\omega^3 \varepsilon^4 p_0} \int_0^L \sum_{f_1} \sum_{f_2} \sum_{f_3} \sum_{f_4} \{\chi^{(4)} S_{f_1,f_2,f_3,f_4,h} (A_{f_1}^{\omega}, A_{f_2}^{\omega}, A_{f_3}^{\omega}, A_{f_4}^{\omega}) \exp(-i\partial\beta_{f_1,f_2,f_3,f_4,h} L)\} dz \quad \text{(A.9)}$$

$$A_{h,y}^{4\omega}(x) = -i \frac{\varepsilon_0 (\beta_f^{\omega})^4}{\omega^3 \varepsilon^4 p_0} \sum_{f_1} \sum_{f_2} \sum_{f_3} \sum_{f_4} \chi^{(4)} S_{f_1,f_2,f_3,f_4,h} (A_{f_1}^{\omega} A_{f_2}^{\omega} A_{f_3}^{\omega} A_{f_4}^{\omega}) \left[\frac{1 - \exp(-i\partial\beta_{f_1,f_2,f_3,f_4,h} L)}{\partial\beta_{f_1,f_2,f_3,f_4,h}} \right] . \quad \text{(A.10)}$$

It is also possible to express the increment in the amplitude of FTH fields along the z-axis by utilising the following integral:

$$A_{h,y}^{5\omega}(x) = -i \frac{\varepsilon_0 (\beta_f^{\omega})^5}{\omega^4 \varepsilon^5 p_0} \int_0^L \sum_{f_1} \sum_{f_2} \sum_{f_3} \sum_{f_4} \sum_{f_5} \{\chi^{(5)} S_{f_1,f_2,f_3,f_4,f_5,h} (A_{f_1}^{\omega}, A_{f_2}^{\omega}, A_{f_3}^{\omega}, A_{f_4}^{\omega}, A_{f_5}^{\omega}) \exp(-i\partial\beta_{f_1,f_2,f_3,f_4,f_5,h} L)\} dz \quad \text{(A.11)}$$

$$A_{h,y}^{5\omega}(x) = -i \frac{\varepsilon_0 (\beta_f^{\omega})^5}{\omega^4 \varepsilon^5 p_0} \sum_{f_1} \sum_{f_2} \sum_{f_3} \sum_{f_4} \sum_{f_5} \chi^{(5)} S_{f_1,f_2,f_3,f_4,f_5,h} (A_{f_1}^{\omega} A_{f_2}^{\omega} A_{f_3}^{\omega} A_{f_4}^{\omega} A_{f_5}^{\omega}) \left[\frac{1 - \exp(-i\partial\beta_{f_1,f_2,f_3,f_4,f_5,h} L)}{\partial\beta_{f_1,f_2,f_3,f_4,f_5,h}} \right] \quad \text{(A.12)}$$

$S_{f_1,f_2,f_3,f_4,h}$ and $S_{f_1,f_2,f_3,f_4,f_5,h}$ are the overlap integral, and they are given by

$$S_{f_1,f_2,f_3,f_4,h} = \int_{-d/2}^{d/2} H_{f_1,y}^{\omega}(x) H_{f_1,y}^{\omega}(x) H_{f_1,y}^{\omega}(x) H_{f_1,y}^{\omega}(x) E_{h,y}^{4\omega}(x) dx \quad \text{(A.13)}$$

$$S_{f_1,f_2,f_3,f_4,f_5,h} = \int_{-d/2}^{d/2} \frac{H_{f_1,y}^{\omega}(x) H_{f_1,y}^{\omega}(x)}{H_{f_1,y}^{\omega}(x) H_{f_1,y}^{\omega}(x) H_{f_1,y}^{\omega}(x) E_{h,y}^{5\omega}(x)} dx \quad \text{(A.14)}$$

Here $E_{h,y}^{m\omega}(x) = 2\sqrt{\frac{m\omega\mu_0}{\beta_{h\infty}^{m\omega} d}} p_0 sc(h\frac{\pi}{d}x)$ and

$$H_{f_1,y}^{\omega}(x) = 2\sqrt{\frac{\omega\varepsilon}{\beta_{f_1\infty}^{\omega} d}} p_0 sc(f_1\frac{\pi}{d}x)$$

$$S_{f_1,f_2,f_3,f_4,m} = 64\sqrt{\frac{\mu_0}{\beta_{f_1\infty}^{\omega}\beta_{f_2\infty}^{\omega}\beta_{f_3\infty}^{\omega}\beta_{f_4\infty}^{\omega}\beta_{h\infty}^{4\omega}}} (\frac{\omega p_0}{d})^{5/2} \varepsilon^2 \int_{-d/2}^{d/2} sc(f_1\frac{\pi}{d}x) sc(f_2\frac{\pi}{d}x) sc(f_3\frac{\pi}{d}x) sc(f_4\frac{\pi}{d}x) sc(h\frac{\pi}{d}x) dx \quad \text{(A.15)}$$

$$S_{f_1,f_2,f_3,f_4,f_5,h} = 64\sqrt{\frac{5\mu_0}{\beta_{f_1\infty}^{\omega}\beta_{f_2\infty}^{\omega}\beta_{f_3\infty}^{\omega}\beta_{f_4\infty}^{\omega}\beta_{f_5\infty}^{\omega}\beta_{h\infty}^{5\omega}}} (\frac{\omega p_0}{d})^{3} \varepsilon^{5/2} \int_{-d/2}^{d/2} sc(f_1\frac{\pi}{d}x) sc(f_2\frac{\pi}{d}x) sc(f_3\frac{\pi}{d}x) sc(f_4\frac{\pi}{d}x) sc(f_5\frac{\pi}{d}x) sc(h\frac{\pi}{d}x) dx \quad \text{(A.16)}$$

References

[1] R. L. Sutherland, Handbook of Nonlinear Optics (Marcel Dekker, Second Ed., New York, 1996).

[2] R. W. Boyd, Nonlinear Optics (Academic Press, Second Ed. 2003).

[3] D. Eimerl, IEEE Journal of Quantum Electronics **23**(8), 1361 (1987).

[4] B. A. Hooper, D. J. Gauthier, J. M. J. Madey, Appl. Opt. **33**(30), 6980 (1994).

[5] S. Akhmanov, A. Dubovik, S. Saltiel, I. Tomov, V. Tunkin, Soviet Journal of Experimental and Theoretical Physics Letters **20**, 117 (1974).

[6] X. Chen, Y. Chen, Y. Xia, Applied Optics **44**(6),

1028 (2005).
[7] G. D. Boyd, C. K. N. Patel, Applied Physics Letters **8**(12), 313 (1966).
[8] H. Komine, W. H. Long, J. W. Tully, E. A. Stappaerts, Opt. Lett. **23**(9), 661 (1998).
[9] M. Raybaut, A. Godard, A. Toulouse, C. Lubin, E. Rosencher, Opt. Express **16**(22), 18457 (2008).
[10] David N. Nikogosyan, Nonlinear Optical Crystals: A Complete Survey, Springer, pp. 5–54, 2005.
[11] Zhenyu Zhang, Bo Wang, Nianmin Zhang, Chaoge Xu, "High-efficiency super-smooth chemical mechanical polishing method for lithium niobate crystal" Publication of CN103978406A, China. Application CN201410197096.5A, Application publication date: 2014/08/13.
[12] S. Kumar, G. Singh, V. Janyani, O. Buryy, U. Serhij, S. Dmytro, M. Tiwari, MgO Doped Lithium Niobate Waveguides Based All Optical Modulator, in Optical and Wireless Technologies, V. Janyani, M. Tiwari, G. Singh, and P. Minzioni, eds., Lecture Notes in Electrical Engineering (Springer Singapore, 2018), **472**, 177.
[13] B. Medhi, S. Deb, Optik **135**, 426 (2017).
[14] J. Saha, S, Deb, Optoelectron. Adv. Mat. **17**(9-10), 430 (2023).
[15] A. Yariv, IEEE J. Quantum Electron. **9**(9), 919 (1973).
[16] R. M. A. Azzam, N. M. Bashara, Ellipsometry and Polarized Light, North Holland Publishing Company, 1977.
[17] M. Saha, S. Deb, P. K. Mandal, B. Medhi, A. Saha, Opt. Express **60**(6), 066104 (2021).
[18] A. W. Snyder, J. D. Love, Applied Optics **15**(1), 236 (1976).
[19] N. Bloembergen, P. S. Pershan, Phys. Rev. **128**(2), 606 (1962).
[20] M. Raybaut, A. Godard, A. Toulouse, C. Lubin, E. Rosencher, Appl. Phys. Lett. **92**(12), 121112 (2008).
[21] J. Saha, S. Deb, Optik **254**, 168689 (2022).
[22] J. Alda, "Laser and Gaussian Beam Propagation and Transformation," in Encyclopedia of Optical and Photonic Engineering (Print) - Five Volume Set, 2nd ed., Boca Raton: CRC Press, pp. 1193–1207, 2015.
[23] B. Saha, N. Goswami, A. Saha, Applied Optics **60**(23), 7027 (2021).
[24] B. Saha, N. Goswami, A. Saha, Applied Optics **61**, 10408 (2022).
[25] A. Andrushchak, O. Buryy, N. Andrushchak, Z. Hotra, O. Sushynskyi, G. Singh, V. Janyani, I. Kityk, Appl. Opt. **56**, 6255 (2017).
[26] D. Sugak, I. I. Syvorotka, U. Yakhnevych, O. Buryy, N. Martynyuk, S. Ubizskii, Ya. Zhydachevskyy, A. Suchocki, H. Kumar, V. Janyani, G. Singh, Acta Physica Polonica A **133**(4), 965 (2018).
[27] Z. Ge, Z. Zhou, Y. Li, C. Yang, S. Liu, B.-S. Shi, Optics Letters **46**, 158 (2021).
[28] K. Stoll, J.-J. Zondy, O. Acef, Opt. Lett. **22**(17), 1302 (1997).
[29] J. Niamtu, Am. J. Cosmet. Surg. **18**, 71 (2001).
[30] R. Tulsawani, P. Sharma, N. K. Sethy, P. Kumari, L. Ganju, S. Prakash, S. Chouhan, PLoS One **15**, e0230175 (2020).
[31] M. Dobber, R. Voors, R. Dirksen, Q. Kleipool, P. Levelt, Solar Physics **249**(2), 281 (2008).
[32] W. G. Telford, S. A. Babin, S. V. Khorev, S. H. Rowe, Cytometry Part A: The Journal of the International Society for Advancement of Cytometry **75**(12), 1031 (2009).
[33] P. Avci, A. Gupta, M. Sadasivam, D. Vecchio, Z. Pam, N. Pam, M. R. Hamblin, Semin. Cutan. Med. Surg. **32**(1), 41 (2013).

*Corresponding author: jayasaha2013@gmail.com